A Relationship Between Transition Region Brightenings, Abundances, and Magnetic Topology

Lyndsay Fletcher† (fletcher@sag.lmsal.com)
Lockheed Martin Solar and Astrophysics Lab., Org L9-41, B252, 2351 Hanover Street, Palo Alto CA 94306, US

Marcelo C. López Fuentes (lopezf@iafe.uba.ar) and Cristina H. Mandrini (mandrini@iafe.uba.ar)
Instituto de Astronomía y Física del Espacio, IAFE, CC67, Suc 28, 1428 Buenos Aires, Argentina

Brigitte Schmieder (brigitte.schmieder@obspm.fr) and Pascal Démoulin (pascal.demoulin@obspm.fr)
Observatoire de Paris, 92195 Meudon, Cedex Principal, France

Helen E. Mason (h.e.mason@damtp.cam.ac.uk)
Department of Applied Mathematics and Theoretical Physics, Cambridge University, Silver Street, Cambridge CA, UK

Peter R.Young (pyoung@cfa.harvard.edu)
Harvard Smithsonian Center for Astrophysics, 60 Garden St., Cambridge, MA 02138, USA

Nariaki Nitta (nitta@notung.lmsal.com)
Lockheed Martin Solar and Astrophysics Lab., Org L9-41, B252, 2351 Hanover Street, Palo Alto CA 94306, US

Sept 18 2000

Abstract. We present multi-instrument observations of active region (AR) 8048, made between June 3 and June 5, 1997, as part of the SoHO Joint Observing Program 33. This AR has a sigmoid-like global shape and undergoes transient brightenings in both soft X-rays and transition region (TR) lines. We compute a magneto-hydrostatic model of the AR magnetic field, using as boundary condition the photospheric observations of SoHO/MDI. The computed large-scale magnetic field lines show that the large-scale sigmoid is formed by two sets of coronal loops. Shorter loops, associated with the core of the SXT emission, coincide with the loops observed in the hotter CDS lines. These loops reveal a gradient of temperature, from 2 MK at the top to 1 MK at the ends. The field lines most closely matching these hot loops extend along the quasi-separatrix layers (QSLs) of the computed coronal field. The TR brightenings observed with SoHO/CDS can also be associated with the magnetic field topology, both QSL intersections with the photosphere, and places where separatrices issuing from bald patches (sites where field lines are tangent to the photosphere) intersect the photosphere. There are, furthermore, suggestions that the element abundances measured in the TR may depend on the type of topological structure present. Typically, the TR brightenings associated with

† Now at Department of Astronomy and Astrophysics, University of Glasgow, Glasgow G12 8QQ, UK

QSLs have coronal abundances, while those associated with BP separatrices have abundances closer to photospheric values. We suggest that this difference is due to the location and manner in which magnetic reconnection occurs in two different topological structures.

Keywords: Magnetic Fields: models, Sun: corona, transition region, bright points, abundances

1. Introduction

Even simple solar active regions pose many questions, regarding their formation, structure and evolution. In this work, we present observations made during a three-day study of AR 8048, using space- and ground-based instrumentation. The analysis of the coronal and transition region (TR) manifestations of this AR, coupled with the modelling of the magnetic field illuminates many aspects of the evolution of the AR, both on the scale of the large loops and small scale brightenings.

The Joint Observing Program 33 (JOP 33) was an observing campaign of the Solar and Heliospheric Observatory (SoHO) that ran between June 3 and June 5, 1997. It involved the Coronal Diagnostic Spectrometer (CDS) (Harrison et al. 1991), the Extreme Ultraviolet Imaging Telescope (EIT) (Delaboudinière et al. 1995) and the Michelson Doppler Interferometer (MDI) (Scherrer et al. 1995). Also participating in this campaign were the Soft X-ray Telescope (SXT) on board Yohkoh (Tsuneta et al. 1991, Ogawara et al. 1991) and the Bialków Hα telescope in Poland. This group of instruments provided us with plasma diagnostics, magnetic field measurements, and high and low temperature images of AR 8048.

AR 8048 was a well-isolated region with a sigmoidal appearance, i.e. on the large scale its loops had a sinuous form. Such sigmoidal features, it was suggested by Nakagawa et al. (1971), were loops with a high twist or helicity. Rust and Kumar (1996) and Hudson et al. (1998) found that, in many cases, the ejection of coronal material (as observed by Yohkoh/SXT) is associated with bright sigmoids, which evolve into arcades of bright loops and which may undergo several eruptions, indicating the release of stored magnetic energy. In fact, repeated eruptions were observed in AR 8048. However, as is described in Sect. 4.2, the sigmoidal shape of the large-scale loops in our AR can be matched well by a nearly potential model. This suggests that the large-scale sigmoidicity of this AR may not be a sign of helicity, but of complexity of the magnetic configuration.

The CDS spectroheliograms reveal a characteristically dynamic TR, with sources varying on the most rapid timescales studied (10-20 minutes). Some of these sources can be readily associated with hotter coronal structures, for example mapping the ends of core SXT loops (as in the case of Mg IX 368.1Å at 1MK), but in lines formed in the temperature range 0.4MK to 0.8MK the emission often occurs in locations having no clear coronal counterpart. This emission is sometimes in the form of compact sources, only 2-3 CDS pixels across; sometimes in long, narrow emission patterns. This looks quite unlike what is seen at higher temperatures (see for example Fig. 4).

Our CDS data include a number of lines from ions of Mg and Ne, providing the opportunity to investigate the Mg/Ne abundance ratio. Mg and Ne are examples of low and high first ionisation potential ions (FIPs of 7.6 and 21.6 eV, respectively). It has been known for some time that the abundances of low FIP relative to high FIP ions is higher in the corona than in the photosphere (Meyer 1985a, b). Spatially resolved spectral observations show that coronal values of the ratio are found in spiky structures extending outwards from the strong magnetic fields of ARs - possibly the base of coronal loops - while photospheric values are found in (morphologically different) strong isolated TR brightenings (Young & Mason 1997, Sheeley 1996).

The brightness distribution at various temperatures, and possibly also the element abundances, are likely to be linked to the magnetic configuration, since the magnetic field determines the channels for plasma and energy transport. Motivated by this, we compute the coronal magnetic field from MDI magnetograms and study the magnetic topology, both loop shapes and the locations of critical structures in the field such as "bald patches" and "quasi-separatrix layers", which are important for understanding magnetic reconnection.

The conventional view of magnetic reconnection is mainly based on the 2-D picture of an X-type neutral point, or its extension to 3-D. It is thought to be accompanied by flux transport across separatrices, where the field-line mapping is discontinuous. But magnetic reconnection can also occur in two other topologies, as described below.

In the first configuration, field lines coming from the corona, touch tangentially the photospheric inversion line and then go back into the corona. Due to the characteristic concave pattern of these lines, Titov et al. (1993) called these photospheric segments 'bald patches' (BPs). Early examples of BPs were given by Seehafer (1986). Secondly, since many magnetic configurations give rise to flares without showing clear evidence for separatrices, the concept of separatrices has been generalised to "quasi-separatrix layers" (QSLs), defined as regions where the magnetic field-line linkage changes drastically (Démoulin et al. 1996).

In recent years, the relationship between magnetic separatrices and solar emission has been usefully explored in various wavelength regimes.

In non-flaring regions, Sakurai & Wang (1999) and Wang et al. (1999) found that SXT loops and Hα plage emission are closely associated with the locations of magnetic separatrices, which are likely to be the site of current heating (as, for example, in the minimum current corona model of Longcope 1996). Not surprisingly, separatrix structures are also important in understanding active phenomena, on all scales. On the very smallest scales, van Ballegooijen et al. (1998) found a relationship between the predicted locations of separatrices between photospheric flux elements and G-band bright points, while Mandrini et al. (1999a, 1999b) related (in particular) BP separatrices to the evolution of Hα fibrils and surges. Aulanier et al. (1998b) found a close correspondence between BP separatrices and Hα and soft X-ray emissions in a small flare. Magnetic reconnection at QSLs has been shown to be at the origin of the energy release in a large variety of events ranging from X flares (e.g. Gaizauskas et al. 1998), to small X-ray bright points (Mandrini et al. 1996) and even to very low energy events associated with radio noise storms and faint brightenings observed by TRACE (Bentley et al. 2000).

Emission in the UV and EUV part of the spectrum has, to our knowledge, been little explored in this respect. In the UV part of the spectrum, Aulanier et al. (1999) studied a filament with SoHO/SUMER, and found Si IV brightenings, indicating energy release at the locations of computed BP separatrices. However, such studies have not been made for the TR, shown by the spectroheliographic measurements of SoHO/CDS to be a highly structured and dynamic region.

In this paper we will continue in the vein of studying the association of solar emission and magnetic structures, emphasizing the relationship of TR brightenings and magnetic topology. By reconstructing the magnetic environment of the AR, we have been able to find a relationship between the high temperature coronal emission in the core of the active region and QSLs, and between TR brightenings and the intersection of QSLs or BP separatrices with the photosphere. We further find that the type of magnetic structure (i.e. a QSL or BP separatrix structure) may affect the local chemical abundances.

The paper is structured in the following way. In §2 we describe the AR and its evolution, in §3 we present the small-scale behaviour of AR 8048 observed by CDS and in §4 the results of the CDS plasma diagnostics, focusing our discussion on the abundance computations. In §5 we compute the coronal magnetic field and its topology, based on MDI magnetograms on each of the three days of observation. We relate the CDS observations to the magnetic topology of the AR. The most probable physical origin of the observed brightenings is also discussed in §5. The final section presents our conclusions.

2. The Structure and Evolution of AR 8048

2.1. Generalities

AR 8048 appeared at the East limb on May 30, 1997, presumably having emerged some time during the preceding half-rotation. The remnant of this AR, considerably decayed, (in particular, without sunspots) is present in the next solar rotation. Several "eruptive" events, occuring as a sudden brightness enhancement, and distortion of the loops or appearance of a 'cusp' structure, were observed in SXT data (see movie at **http://www.astro.gla.ac.uk/ lyndsay/JOP033/sxt.mpeg**). On June 1, two optical sub-flares were seen in H_α, while on June 2, 3 and 5 filament disappearance events took place. However, there was no significant GOES activity (class B flares or higher) attributed to this AR.

2.2. The Coronal Sigmoid Appearance

At the time of its appearance, AR 8048 consisted of a main and a small trailing bipole (see Fig. 1). The SXT loop system appears sigmoidal, with loops joining the two polarities of the leading bipole forming the top part of the 'S', and larger, fainter loops, joining the negative polarity of the leading bipole with the positive polarity of the smaller bipole, forming the bottom part of the 'S'. This is in agreement with the independent study of Glover et al. (2000) who classified the AR as "projected-sigmoidal", meaning that the AR comprises many loops, the projection of which onto the disk causes them to appear sigmoidal. However, at various times the core SXT loops, lying between the polarities of the main bipole, also have a slight 'S' shape, apparently without being composed of different systems of loops (Fig. 3). This could be indicative of twist, though of a very low value as shown by the magnetic field model in Section 4.2.

Individual loops or groups of loops brighten and dim on timescales of tens of minutes. It seems plausible that this happens as the magnetic elements in which they are rooted merge, reconnect and split as they are buffeted by convective cells. According to our results in Section 4.3, this reconnection process may occur at QSLs.

2.3. The Photospheric and Chromospheric Description

During the three days of CDS observations, the magnetic flux stayed constant while the area increased, which is a sign that the AR is in its decay phase (van Driel-Gesztelyi 1998). The leading spot is surrounded by a moat region, which consists of bipolar elements moving radially away from the main field (moving magnetic features) with the outer edge having the same polarity as the sunspot (Fig. 2). The trailing spot does not exhibit this behaviour, though both positive and negative flux concentrations undergo several changes near the southern edge of the spot, e.g. the positive flux breaking off from the trailing spot is advected clockwise and southwards around this spot (Fig. 2). A movie of the region made from MDI hourly magnetograms can be seen at **http://www.astro.gla.ac.uk/ lyndsay/JOP033/mdi.mpeg**. It reveals a great deal of splitting and merging activity in this small-scale field, with typical magnetic elements (on a scale of $\sim$ 20") retaining their identities for a timescale of a few hours before the next merging, splitting or disappearance. Some of these changes are reflected in small-scale intensity variations observed by CDS in low temperature lines.

Bialków Hα telescope provided filtergrams with 0.5 Å bandpass for the 3 days (Fig. 2). The fibrils around the trailing spot present a marked clockwise direction, which is indicative of the sign of the twist in the loops (see Section 4.2). On June 5, we observed the formation of a filament between the main bipole and the trailing bipolar field.

3. CDS Observations

3.1. Coronal Brightenings

In this section we study the physical properties of AR 8048 on a small scale, using SoHO/CDS data. Spectroheliograms of the AR in a number of lines formed at different temperatures are used to derive abundances and densities, and form a picture of the system at different temperatures.

The CDS field of view covers most of the central portion of AR 8048 on June 3 and 4, and about half of it on June 5 (Fig. 3). We ran two programs - TRANREG and TREG22. TRANREG consists of 5 or 6 rasters, each lasting 10 minutes, and using a pixel size of 2."0 $\times$ 1."7, in a few strong, well-isolated lines with formation temperatures spanning the range 20,000K to 2MK. The TREG22 rasters take approximately 45 minutes, with a pixel size of 4."0 $\times$ 1."7, in a range of lines spanning TR and low coronal temperatures. In particular, a series of lines from different ionisation stages of Mg and Ne are present. The highest temperature line in this raster is the line of Si XII at 520.6Å with a temperature of maximum ionisation fraction of 2 MK. Emission in this ion tends to occur at the same location as the SXT emission in the core of the AR (Fig. 3). Emission from locations corresponding to the ends of the hot core loops is present in lines of around one million degrees, e.g. Mg IX. This Mg IX emission is probably the hot upper TR of these overlying high temperature SXT loops - or 'moss', as observed at high resolution by TRACE (e.g. Berger et al. 1999, Fletcher & De Pontieu 1999). Elongated Mg IX structures are also present, at a low intensity, suggesting also the presence of longer loops with a temperature around one million degrees.

3.2. Transition Region Brightenings and their Evolution

The distribution of emission in lines of a few hundred thousand K is typically very different from that of lines of 1MK and above. As an example, a comparison between simultaneous rasters in the strong lines of O V 629.7Å at 0.25MK and Mg IX 368.1Å at 1.0MK (Fig. 4) shows how, although some of the emission in the lower temperature lines occurs at the same locations as the million degree emission, much of the TR structure has no coronal counterpart. Further, there is no clear association on this scale between the TR line emission and the photospheric field in the region. Rather than thinking in terms of continuous magnetic loops from photosphere to corona, the key to understanding the bright TR emission may in fact lie in the discontinuities - the separatrix structures in the AR magnetic field.

Because of our interest in abundances, we have focussed this study on lines of Mg (low FIP) and Ne (high FIP) elements. In TR lines of these elements (e.g. Ne IV,V, VI; Mg V, VI, VI), the emission is concentrated into a small number of intense brightenings.

We identify in the first instance 5 strong Ne VI (562.8Å) TR brightenings in the TREG22 raster run at 14:09:19 UT on June 3. These including all pixels around the brightest pixel with intensity in the Ne VI (562.8Å) greater than 50 ergs $cm^{-2}s^{-1}sterad^{-1}$. These are labeled A-E on Figures 8a and 10. These regions were visible in Ne lines from IV to VI. In Mg V, Features A and C were visible; while Features A, C and E were visible in Mg VI. Line intensities in these TR brightenings vary rapidly. Starting at 15:39:10 UT, raster TREG22 is re-run and considerable changes have taken place. In Table I we present the mean intensity, averaged over a number of pixels, from each of the bright features for both runs of the raster on June 3, obtained by fitting Gaussians plus a constant background to the line profiles averaged over pixels, using χ^2 minimisation software written for the purpose by S. V. Haugan. The counts for each of the features at 15:39:19 UT have been averaged over the rotated pixel locations from the 14:09:19 UT observations, regardless of whether these locations are bright in the 15:39:19 UT raster.

The picture is a dynamic one. In the 90 minutes intervening between the start of each raster. Features A and D dim considerably. The intensity of Feature C increases in all of the observed low temperature lines of Ne and Mg, the increase being higher in the higher temperature lines. There is also a slight increase in Feature E.

On June 4 and 5, Features A, C and D are no longer present; while E is no longer in the FOV of CDS (see Figs. 8(a), 9(a)). The single Mg/Ne feature appearing on June 4 and June 5 is the same as Feature B on June 3, this is further borne out by examining the position of the features relative to the MDI magnetic field on subsequent days. This feature first decreases in intensity on June 4 then increases on June 5 (Table II).

Consider the average intensities in Feature C on June 3 (Table I). At 14:09:19 UT they are in the ratio $\mathrm{I_{NeIV}} : \mathrm{I_{Ne\ V}} : \mathrm{I_{NeVI}} = 1 : 3.0 \pm 0.3 : 5.8 \pm 0.6$. At 15:39:10 UT the ratio is $1 : 3.1 \pm 0.3 : 8.6 \pm 0.9$. High temperature emission has increased relative to low temperature emission. This is also seen in the Mg lines. A similar increase in the ratio of intensities is also seen in the single feature (at the location corresponding to B), between the two rasters on June 5 (Table II). By contrast, the intensity ratios in Feature B are $1 : 2.7 \pm 0.3 : 6.3 \pm 0.7$ and $1 : 3.0 \pm 0.3 : 6.3 \pm 0.7$ at the two rasters, showing no variation within the errors. How should we interpret these variations?

The intensity, $I(\lambda_{i,j})$ in ergs cm^{-3} s^{-1} in a given line is given by

$$4\pi I(\lambda_{ji}) = 0.83 \int_L Ab\ \epsilon_{ij}\ n_{\mathrm{e}}\ F(T)\ ds, \tag{1}$$

where s is the line-of-sight column depth (the distance L being determined by the range of temperatures, and hence positions in the atmosphere, over which the line is generated), Ab is the abundance of the element relative to hydrogen, ne the electron number density, F(T) the ionisation fraction for the ion under consideration and 0.83 is the ratio of protons to free electrons. We have defined an ion emissivity, ϵ_{ij} as

$$\epsilon_{ij} = \Delta E\ N_j\ A_{ji} \tag{2}$$

where ΔE is the photon energy, N_j is the fraction of ions in the upper state j and A_{ji} the Einstein coefficient for the transition. For a collisionally excited line (as is normally assumed to be the case in the optically-thin corona) N_j depends on the plasma temperature and n_{e}. So the observed variations in intensity may be due to changes in density, or temperature, or in the abundance of the emitting element.

However, by considering ratios of lines from different ionisation stages of the same element, the abundance factors drop out, while the only density dependence lies in the ratios of the $\epsilon_i j$. For the sequences of magnesium and neon ions considered here, we have used the CHIANTI (v2.0) database (Dere et al. 1997, Landi et al. 1999) to calculate ϵ_{ij} as a function of n_e for the lines that we use, and find the ratios from the different ionisation stages vary only be a few percent over the density range $10^9 - 10^{11}$ cm^{-3}. Thus the ratios of emission lines from different ionisation stages of the same element are only sensitive to the distribution of plasma with temperature, and we attribute the observed intensity variations within ions of a single element as primarily due to temperature changes. When comparing lines from different elements, however, one needs to take into account Ab, n_e and T.

3.3. Determination of Mg/Ne abundance ratios using line ratios

We carry out abundance determinations in each of the bright Ne/Mg features, using two different methods. The first is the line ratio method presented in Young & Mason (1997). Examples of the spectra used for this work are shown in Figure 5.

Writing

$$G(T) = \frac{0.83\ n_j\ A_{ji} F(T)}{n_e}, \tag{3}$$

Eq. 1 becomes

$$4\pi I(\lambda_{ij}) = Ab \Delta E \int_L G(T)\ n_{\mathrm{e}}^2\ ds \tag{4}$$

where $G(T)$ is called the contribution function. The line intensity method relies on the fact that the temperature dependence of the $G(T)$ functions for the Mg VI 349.2 Å and Ne VI 562.8Å lines is very similar. In particular, the excitation peak occurs at the same temperature of $\log_{10}(T_e)$= 5.62. If it can be assumed that the emission is occuring in locations where the plasma is at, or very near this peak temperature, and that both lines are emitted by the same volume of plasma, then we can remove the temperature dependence. The ratio of the measured intensities is then directly proportional to the ratio of the elemental abundances.

Under this approximation, the intensity ratio depends on the line emissivities $\epsilon_{349.2}, \epsilon_{562.8}$, the ratio Q of the ionisation fractions of each ion (calculated at temperature of maximum ionisation fraction), and the abundance ratio $\mathrm{R}_{\mathrm{Mg/Ne}}$;

$$\frac{\mathrm{I}_{349.2}}{\mathrm{I}_{562.8}} = \frac{\epsilon_{349.2}}{\epsilon_{562.8}}\ Q\ \mathrm{R}_{\mathrm{Mg/Ne}}. \tag{5}$$

Q was estimated by Young & Mason to have the value 1.22 (on the basis of the Arnaud and Rothenflug (1985) ionisation equation). The ratio of line emissivities, calculated by summing together contributions from two close Mg VI lines at 349.17 and 349.18 Å, and two Ne VI lines at 562.71 and 562.80 Å, at their temperature of maximum ionisation fraction, varies somewhat with density (Figure 6). The variation is by no more than 15% over the expected (or measured) range of TR densities in our sources, of $10^9 - 10^{10}\mathrm{cm}^{-3}$, however we must have a means of measuring density.

The density can be derived from a diagnostic formed by the lines of Mg VII at 319.0 and 367.7 Å. Although this diagnostic is for slightly higher temperatures ($\log_{10}(T_e)$= 5.8) than the formation temperature of the Mg VI and Ne VI ions ($\log_{10}(T_e)$= 5.6), there is a strong Mg VII component at the locations of the Ne VI/Mg VI sources, and we expect it will give a good idea of the local density. The theoretical density dependence of the Mg VII ratio is shown in Figure 7. Mg VII 367.7 Å is close to the stronger Mg IX line at 368.1 Å and must be fitted simultaneously with a double Gaussian. Mg VII 319.0 Å appears well-separated, but is blended with a strong high temperature line of Ni XV (2.5 MK). Therefore, it can only be measured with confidence in regions where high temperature emission is negligible. The derived value of the density for Feature D, which is also the site of (overlying) emission in SXT and Si XII wavelengths, is therefore an upper limit.

The Mg/Ne intensity ratios in Features A-E are presented in Table III, along with the Mg VII intensity ratio, the electron density and the ratio of Mg to Ne abundances. Note, the densities and abundances have been calculated: (a) using a blanket 25% error value, to take into account the expected errors in the atomic data, which are typically greater than the observational errors (which are of the order 10 - 15%), and (b) using the updated CDS NIS detector calibrations of 23-Dec-98. This contrasts with the density and abundance values calculated by Young & Mason (1997) since that work dates from before the new detector calibrations were announced. The abundance values calculated using the new calibrations are roughly 0.6-0.7 times that of the values which would be calculated using the old values (dependent on electron density in the feature).

3.4. Evolution of Mg/Ne abundance ratios

Our derived abundance ratios range between 1 and 3. In none of the features is the abundance ratio $R_{\mathrm{Mg/Ne}}$ as low as the photospheric value (reported as 0.26±0.05 by Young & Mason 1997) in a low-lying TR feature, which they associated with flux emergence. The coronal ratio found by Young & Mason was 2.4$\pm$0.3 with the old calibrations, or ~ 1.7 with new calibrations. Our abundance values are thus all nearer coronal than photospheric values. Densities in each of the features, from the Mg VII density diagnostic, are consistent with normal coronal values of a few $\times 10^{9}\mathrm{cm}^{-3}$.

Between the two June 3 rasters there are considerable changes in the value of the average abundance ratio, the most striking being the increase in the ratio in Feature C from 2.3 ± 0.5 to 3.2 ± 0.7, and in Feature E from 2.5 ± 0.5 to 3.9 ± 0.3. In the former case, the change is associated with evidence of heating, contrary to Feature E, where $R_{\mathrm{Mg/Ne}}$ increases apparently without any heating taking place. There may in fact be some cooling. In Features B and D the abundances remain more-or-less the same, as do the ratios of intensity in the Ne lines. Note that in Feature D there is co-spatial high temperature emission which may have resulted in artificially high density measurements. This in turn may have led to the emissivity ratio being overestimated by $\sim 15\%$, and the abundance ratio underestimated by a corresponding amount.

On June 4 and 5, $\mathrm{R_{Mg/Ne}}$ for the single feature (which would correspond to Feature B) varies strongly, first decreasing from 1.1 ± 0.3 to 0.7$\pm$0.2 on June 4, then increasing from 0.8$\pm$0.2 to 1.2 ± 0.3. The increase is associated with an increase in temperature, as shown by the ratio of the low T Mg and Ne lines.

In summary, from feature to feature (and also within features, though we do not illustrate this here) there is no apparent correlation between n_e and the abundance ratio, neither do the rapidly varying abundance ratios systematically track temperature variations. But there are significant abundance variations, and we wish to stress in particular that, out of all the features observed on June 3, B and D are the ones having the lowest abundance ratio on both rasters. In Section 5, we attempt an explanation of this fact based on the results of our topological analysis (Sect. 4.3).

3.5. Determination of Mg/Ne abundance ratios using emission measures

The abundance variations between sources derived above are not large, and it is possible that they are an effect of temperature. Recall that in using the line ratio method we assume that the form of the $G(T)$ curves for each ion is sufficiently similar that the contributions as a function of temperature to the total emission are distributed in the same way. This is not the case; over the temperature range $\log_{10}(T_e)$= 5.2 to 5.8 the ratio $G(T)_{\mathrm{MgVI}}/G(T)_{\mathrm{NeVI}}$ varies between 0.4 and 1.5. However, we can examine the influence of temperature by looking at the emission over a number of lines formed at a range of temperatures.

If we assume that a spectral line is emitted over a temperature range ΔT around its temperature of peak formation $T_{\max}$, then we can approximate $G(T) = const = G_o$ in Eq. 4. G_o is defined as;

$$G_o = \frac{\int G(T)dT}{T(10^{0.15} - 10^{-0.15})} = \frac{\int G(T)dT}{0.7\ T_{\max}}. \tag{6}$$

Then $I(\lambda)$ is directly proportional to the product of column emission measure and abundance, as follows.

$$4\pi I(\lambda) = Ab\ \Delta E G_o \mathrm{EM} \tag{7}$$

where the column emission measure to depth L along the line of sight is defined as $\mathrm{EM} = \int_L n_e^2 ds$. The EM derived at each temperature should be the same regardless of the ion which is being used to measure it. By comparing Ab EM $= 4\pi I(\lambda)/G_o\Delta E$ for a number of ions of Mg and Ne we see the effect of abundance . G_o is calculated again using data from the CHIANTI database.

Plots of (scaled) Ab EM(T) are shown in Figures 11. These are divided according to the type of magnetic structure with which each is associated (which will be explained in Sect. 4.3). The difference between the two sets of curves for each source (Mg indicated by diamonds, Ne by triangles) reflects the effect of abundance. Note, the expected dependence of EM on temperature (in a plane-stratified atmosphere where conduction balances radiation) is EM $\sim \mathrm{T}^{3/2}$ (e.g Jordan 1996). We have removed this expected dependence by further dividing through by $T^{3/2}$; the purpose being only to emphasise the abundance variations. The abundance variations seen in this way are also small, however the fact that the lines for sources A, C and E tend to be further offset from each other than those for B and D confirms our initial finding of abundance variations from source to source. The ratios EM $\times$ Ab for Mg VI and Ne VI, at $\log_{10}(T_e)$= 5.6 are in the range 0.8 - 2.8. These ratios are comparable to, but consistently lower than the abundance ratios found with the line ratio method, by a factor $1.4 - 1.6$.

The additional sources F-I shown on these figures are discussed Section 5.

4. The Magnetic Field Environment

4.1. Coalignment of MDI and CDS images

We have coaligned CDS and MDI, with the MDI images rotated to the start time of the CDS spectroheliograms. Generally, over the three analysed days, the Si XII (2 MK) loops in the core of the AR begin and end around the strong leading bipole field but not in the very strongest longitudinal fields ($|B_l| > 500$ G), i.e., not in the sunspots. Rather, the core loops are rooted in weaker plage field of $100 < |B_l| < 500$ G. This agrees with similar results found by Golub et al. (1994), Schmieder et al. (1996) and Deng et al. (1999). Million degree emission in the lines of Mg IX and Ca X is concentrated in blobs around the ends of the Si XII structures. On June 4, elongated million-degree structures - presumably loops - are clearly observed extending southwards from a region where negative and positive fields are in close proximity. This is also the location of brightenings in TR lines (Fig. 9).

MDI movies of the local field (96 min. synoptic cadence) indicate that TR brightenings take place under various conditions of the magnetic field. As an example of this variety, take the first CDS observations made on June 3, at 14:09:19 UT, in the Ne VI 562.4 Å (Fig. 8a). We pick three of the five identified brightenings, Features B, A and D. Brightening B is in a region where positive spot field and negative plage field are close to one another. Brightening A is well inside the trailing positive polarity of the main bipole. The third brightening, D, is also in a positive field region which is in the process of dividing in two. It is therefore not clear that the brightenings are always related to flux emergence, for example, or always to magnetic cancellations at the photosphere.

4.2. Modelling the AR Magnetic Field

We have modelled the magnetic field of the AR applying a linear magnetohydrostatic (LMHS) approach, developed by Low (1991, 1992). In a cartesian (x,y,z) system of coordinates this leads to the following equation:

$$\vec{\nabla} \times \vec{B} = \alpha \vec{B} + f(z) \vec{\nabla} B_z \times \vec{u}_z \tag{8}$$

where α is taken to be a constant and $f(z) = a \exp(-z/H)$. In this way, the interaction between the magnetic field and the plasma is taken into account. The z axis is chosen to be normal to the photosphere, with $z = 0$ at the photospheric level. In all our models we have used $a = 1$ and $H = 5$ Mm. The numerical calculation consists of a extrapolation of the longitudinal photospheric magnetic field, as observed by MDI, to a finite volume region in $z > 0$ (see e.g. Aulanier et al. 1998b, Mandrini et al. 2000, López Fuentes et al. 2000).

Once a and H are chosen, the model depends on the free parameter α. As a first approach, we have determined the value of α in such a way that the computed coronal field lines match (by an eyeball comparison) the shape of the loops observed by SXT in images taken on times close to the MDI magnetograms. The values of α that give the best fit to the observations are: $\alpha = 0.003$ Mm^{-1} for June 3 and 0.0045 Mm^{-1} for June 4 and 5 (Fig. 1). Notice that the computed field lines follow the global 'S' shape of the SXT loops, however α takes very low values. The observed 'S' shape may in fact, not be an indication of twist, rather of complexity in the photospheric field distribution. The configuration results from the combination of two sets of loops, i.e. it is not a single set of loops which have an 'S' shape. A similar configuration is also found with a potential extrapolation ($a = 0, \alpha = 0$; this implies that there are no currents in the coronal field). We have also investigated whether the value of α could vary with height. We have found that, in order to fit the shape of chromospheric fibrils (see Fig. 2), we have to increase the value of α up to 0.0075 Mm^{-1} for the three days. Doing so, the shorter SXT loops concentrated in the core of the AR (see Fig. 3) were also better represented, the same being true for the Si XII brightenings shown in Figures 8 and 9. Similar results, showing that the magnetic shear may decrease with increasing height, have been found by Schmieder et al. (1996). They showed that, to fit the shape of observed loops, field lines computed at low coronal or chromospheric heights needed a higher α than those at higher heights.

4.3. Magnetic Topology

Following the method of Démoulin et al. (1996), we have computed the locations of QSLs and analysed their relationship to the observed CDS transition region brightenings. QSLs are regions where field lines initially close together separate widely when followed. At the location of separatrices, the magnetic field line linkage is discontinuous, QSLs are a generalisation of the concept of separatrices to configurations without such discontinuities. Therefore, when QSLs are computed we also find the places where separatrices will lie. Separatrices are present in the solar atmosphere in two cases, either when magnetic nulls appear in the configuration or when some field lines are tangentially touching the photosphere (these field lines are curved up at the photosphere). This latter case can happen along portions of the inversion line for the component of the field normal to the photosphere. These portions are called BPs.

Figures 8 and 9 (and a corresponding one for June 5, not shown) show that the topological structure of the AR is globally similar over the three analysed days. QSLs located on the main bipolar field exhibit similar features from day to day. Differences in their distribution are mainly due to the appearance and/or the evolution of parasitic polarities.

BPs are located mainly in two different regions: one, apparent on all days, at the North-East of the leading spot (these we refer to as the northern BPs), and the other, only appearing on June 4 and 5, at the South of the following spot (the southern BPs); see Figs. 8e and 9e. The location and shape of these BPs change according to the evolution of the moving magnetic features in the moat of the leading spot. The separatrices associated with the northern BPs are, on the west side of the BPs, very close to them (lying at a low field region with $|B_l| \approx 20$ G, see Figs. 8c and 9c); while they extend farther away towards the East (up to the zone with $|B_l| > 500$ G). On June 4 and 5 the separatrices corresponding to the southern BPs lie on the low field region ($|B_l| \approx 100$ G) below the following spot, and along the negative field region which extends South-East from the preceding spot. On June 3 there is also a central BP, having one of its separatrices extending in the NW-SE direction (see Fig. 8c and Sect. 4.4). This particular BP is significant in our interpretation of the CDS TR brightenings and abundance variations.

On June 3, we do not find a BP at the corresponding location of the June 4 and June 5 southern BPs (Figs. 8e and 9e), though QSLs resembling the shape of the southern BPs separatrices are present (Figs. 8d). We find that from June 3 to June 4 the positive polarity decreased in flux, while the negative one increased. This change in the relationship between positive and negative flux from June 3 to June 4 is the origin of the appearance of the southern BPs. Nevertheless, we suspect strongly that in reality a BP was present there on June 3, for the following reason. When a parasitic polarity is present in a surrounding field of opposite polarity, the size of the magnetogram pixel has a dramatic effect: there is not only an averaging of the magnetic intensity, but also a cancellation of the parasitic flux with the neighbouring stronger field, since what is measured is the magnetic flux. This effect can delay the appearance of a parasitic polarity in the magnetogram by more than one day (as in the flaring configurations studied by Mandrini et al. 1993 and Aulanier et al. 1998b).

4.4. Relationship between CDS Brightenings and Magnetic Topology

Figures 8 and 9 illustrate the relationship between the locations of BP separatrices or QSLs and Ne VI, Mg IX or Si XII brightenings on June 3 and 4 (both observations and magnetic field topology are very similar between June 4 and 5). We have chosen Ne VI, Mg IX and Si XII for our comparison, due to their difference in formation temperature. Ne VI (resp. Mg IX) emission mainly comes from the low (resp. high) TR, so we expect to observe kernels in these lines close to the footpoints of the magnetic field lines; while, Si XII emission is associated with their coronal portion (see Sect. 3). In order to simplify the figures we have drawn QSLs and BPs, together with their separatrices, only when they lie within the CDS field of view, and occur near the observed CDS emission.

The presumed footpoints of the hot emission seen in Si XII lie near the core of the AR, from the evidence of Mg IX 1 MK emission (Peres et al. 1994, Berger et al. 2000). As shown in Figures 8 and 9 (panels b and d), we find QSLs lying close to the Mg IX brightenings; furthermore, the global shape of the coronal Si XII and SXT emission coincides with the shape of field lines which have footpoints at these QSLs. We also observe that the more diffuse SXT (see Figs. 3) emission can be traced by field lines which have footpoints at the QSLs located on the main bipolar field. So the intense core Si XII emission (outlining the 2 MK plasma) and soft X-ray emission (outlining the 2-6 MK plasma), may be due to energy release at QSLs where current sheets form and heating is likely to take place. Differences in intensity between the core and diffuse SXT emission may be linked to the volume of the magnetic flux tubes involved, and the amount of energy released.

Mg IX and Si XII emission is not observed associated with all separatrix or quasi-separatrix structures. Whether or not it is so may also depend on whether the energy released at reconnection occuring at these structures is enough to heat corona and transition region to sufficiently high temperatures.

Turning now to the cooler emission in the bright Ne VI features, we see that there is a general coincidence in position between these features and the positions of either the intersection of QSLs with the photosphere, or the intersection of separatrices issuing from BPs with the photosphere (note, not at the BPs themselves). Close inspection shows that many of the dimmer elongated features on the Ne VI map are also very near QSLs or BP separatrices; compare Fig. 8 a, c, d, e and Fig. 9 a, c, d, e. In particular, on June 3, Feature D lies directly on top of a BP separatrix from the central BP. The central BP and its separatrix disappear the next day along with feature D. This provides strong evidence for a link between Feature D and the central BP. Also, Feature B, though not obviously on a BP separatrix on June 3, is at a location which on June 4 and 5 clearly shows a BP and separatrix structure, and a persistent Ne VI brightening. §4.3 explains why a BP may already be present on June 3 but not revealed by the extrapolations.

Feature A on June 3 lies close to a separatrix from the North-East BP, and directly on top of a location where QSL field lines intersect the photosphere. Features C and E are close to locations where QSLs intersect the photosphere. Displacements between the BP separatrices or QSLs and the brightenings may have three different origins: an error in the coalignment between CDS and MDI, an error in the computed coronal field, or a physical displacement of the TR features from the BP separatrices or QSLs, as a result of connectivity changes following reconnection.

Summing up, we suggest that many of the bright TR brightenings visible in the Ne VI raster are associated with the intersection of various topological structures with the photosphere. We have found two types of structures; those composed of field lines issuing from a photospheric bald patch, and the more general quasi-separatrix layers (the ones which are not associated with BPs). Features B and D are probably linked to BP separatrices; while Features C, E and some weak emission surrounding Feature B on June 4 and 5 are related to QSLs. Feature A can be linked to either a BP separatrix or to a QSL, as explained above. Features C and E are at the base of large, diffuse SXT loops extending out into the corona and are, thus, consistent with the nature of the Sheeley features and those observed by Young & Mason (1997).

5. Origin of the Ne VI brightenings and abundance variations

The results described above lead us to propose the following physical scenario. Ne VI features are in general a consequence of energy release by magnetic reconnection at separatrices, driven by the continual magnetic field changes observed. Features B and D (and possibly A) are the consequence of energy release by magnetic reconnection occurring at the BP separatrices (considering that on June 3 Feature B is probably also associated with a BP and its separatrix - see the end of §4.3). Features C, E and probably A lie close to the photospheric intersection of QSLs. These brightenings may result from magnetic reconnection at the related QSLs.

The BPs themselves are also locations in which reconnection will occur, but this occurs at a very low height in the atmosphere (chromospheric or even photospheric) and, thus, we might not expect to see TR brightenings right above the BPs. But during BP reconnection, two things might happen. Firstly, part of the energy released is transported along separatrix field lines, as particles or in the form of conduction, causing heating and the evaporation of some chromospheric plasma at the other end. This may cause local brightenings. But secondly, the post-reconnection configuration at BPs, in which field lines which were tangent to the photosphere at the BP and concave up (see e.g. Titov et al., 1993) spring up after reconnection; photospheric material can then be lifted into the atmosphere by the rising BP field lines, and spread out along them. Thus one would expect field lines associated with BPs to exhibit a more photospheric abundance ratio than those which are not.

We do indeed observe a difference in the abundance ratio Mg/Ne between the different sources, and suggest that this may be linked to the different ways magnetic reconnection proceeds in QSLs and BPs. We have found that both Features B and D (associated to BPs) have somewhat lower abundance ratio when compared to typical coronal abundances, while other features (C, E), which are associated with QSLs, have an abundance ratio around the typical coronal value.

The status of feature A is unclear. It is close to both a QSL intersection and a BP separatrix, though closer to the QSL location. If indeed it is associated with a BP separatrix, rather than the nearby QSL, then we must explain why its abundance ratio is higher than the BP sources B and D. Is source A an exception to the association of BPs with low abundance ratios? One explanation may lie in the height of the field lines connecting the BP and the location of the intersection of its separatrix with the photosphere near Feature A. These field lines are long and high, compared to the equivalent field lines ending near sources B and D. The lift-up and transport along the field lines in BP reconnection is likely to be more efficient in short, low lying magnetic lines.

Broadly speaking, it is seen that the Mg/Ne abundance ratio is less than 2 for sources associated with BPs, and greater than 2 for sources associated with QSLs. The small number of sources, A to E, had been identified and studied before the field topology was investigated, but this hint of a relationship between topological structures and abundance ratio prompts us to look at the abundances at fainter sources, coincident with other predicted QSL and BP separatrix structures on June 3 - the full set is indicated on Figure 10. We have defined a further 5 sources, in which the Ne VI (562.8Å) intensity is greater than

30 ergs $cm^{-2}s^{-1}sterad^{-1}$. Using the same analysis method described earlier we find that in another three sources (F, H and J) close to BP separatrix locations $R_{\mathrm{Mg/Ne}}$ is again less than 2. The values are $R_{\mathrm{Mg/Ne}} = 1.7 \pm 0.5$, 1.2 ± 0.3 and 0.8 ± 0.2 respectively. Two further sources, G and I, close to QSLs show (for I) $R_{\mathrm{Mg/Ne}} = 2.7 \pm 0.6$, in line with previous examples, and for G $R_{\mathrm{Mg/Ne}} = 0.9 \pm 0.2$, which does not follow the trend. However, it should be noted that this latter source is also at the location where a BP and BP separatrix appear on the following day, and we may have a situation similar to that of the much stronger source B, which had a low abundance ratio the day before the BP appeared in the computations. With the exception of source G, the ratio of EM $\times$ Ab for Mg VI and Ne VI is again consistently lower by a factor 1.4-1.6 than the abundance ratios found using the line ratio method.

The abundance variations were also studied at different temperatures, as in the case of brightnings A-E. The results are summarised in Figures 11 (a) and (b) which are plotted for BPs and QSLs respectively. Although the differences between the two plots are not large, consistent with the fact that the abundance variations from the line ratio technique are not large, it should be noted that there is a general trend for the Mg and Ne curves (diamonds and squares) to be closer together in the sources near BPs than those near QSLs. This effect is in fact more prominent than the figures show. The values on the Mg curves at $\log_{10}(T_e)= 5.5$ (Mg V) are upper limits in Features D, F, and H (and also in Feature G, which further adds to our suspicion that this was a forming BP separatrix on June 3), since the Mg V line was too faint to measure reliably. This would bring the curves yet closer together in 3 of 5 of the BP features, as well as Feature G. This further analysis supports our contention that the abundance ratios are systematically different near BPs and QSLs, with BPs showing a lower ratio of low to high FIP elements - more photospheric - and QSLs showing a higher ratio.

6. Conclusion

We have presented the analysis of AR 8048 during three days using coordinated observations of SoHO (CDS and MDI), Yohkoh (SXT) and Bialków (Hα telescope). They provide several diagnostics (temperatures, densities, abundances) of the TR and coronal plasma, the longitudinal component of the photospheric field and chromospheric brightness distribution.

At transition region temperatures, this AR presents five bright features on June 3, while only one is observed on the next two days. Densities in the strong Ne VI features, measured with CDS line ratio diagnostics, are consistent with normal TR values and remain constant from pixel to pixel, within the errors. Features A, C and E have Mg/Ne abundance ratio as high as previously measured for coronal structures, while features B and D have a somewhat lower abundance ratio (but still above typical photospheric value). The average Mg/Ne abundance ratio in bright sources, varies with time by up to 80%, and there are also pixel-to-pixel variations in the ratio. The elemental abundance ratios have long been known to vary in solar flares (cf. Lin 1987) and it has been proposed, for example, that selective acceleration of ions on the basis of charge-to-mass may occur by waves generated in reconnection events (Miller & Viñas 1992). We propose an alternative, linked to magnetic reconnection.

The coalignment of the CDS and Yohkoh data with MDI, together with the computation of the coronal magnetic field and its topology have shown the relationship between the emissions at various temperatures (TR and coronal), and the magnetic field topology. At coronal temperatures, the Si XII emission, at the core of the AR, is related to the high transition region Mg IX brightenings lying on QSLs. Field lines starting from these QSLs follow the shape of the Si XII emission. The most diffuse SXT emission is also related to magnetic lines linking QSLs at the main bipolar field. Many features which are bright in the TR line of Ne VI lie close to the photospheric intersection of topological structures, both BP separatrices and QSLs. These topological structures are locations where energy release is likely to take place, in the form of heating at current sheets for example. The narrow, elongated appearance of the TR brightenings is consistent with the photospheric intersection of these structures. The disappearance of one of the TR features, feature D, is simultaneous with the disappearance of its associated BP and BP separatrix.

We have further noted abundance differences between the TR features observed in Ne VI, and suggest a possible origin for this. Features C, E, and (most likely) A are found to be associated with QSLs and have $R_{\mathrm{Mg/Ne}} > 2$. These TR and coronal brightenings have most probably their origin in the release of magnetic energy by reconnection at the QSLs, as described in the model of Démoulin and Priest (1997). Features B, and D are rather found associated with a particular magnetic topology formed by field lines which are tangent to and curved up above the photosphere (at BPs). Both Feature D and the corresponding BP, present on June 3, disappear the next days. Magnetic reconnection in a BP topology, not only releases energy, but allows the lifting-up of photospheric or chromospheric material (e.g. Titov et al. 1993, Cheng and Choe 1998) which has typically a lower abundance ratio than coronal plasma. The action of BP reconnection may therefore lead to the more chromospheric abundance ratio observed in BP-associated brightenings. The observed differences in abundance ratio between features may therefore be due to the magnetic topology involved. This tendency is broadly confirmed by a further four fainter sources (F to I). It should be noted that in source G, apparently associated with a QSL, the abundance ratio is low. However, the following day, a BP separatrix has appeared at the same location.

It is certainly worthwhile analysing a much larger set of events before drawing a firm conclusion, yet the present results can serve as a guide to constrain further the possible processes which may lead to an abundance segregation. There is further work to be done; for example, we observed a correlation between the increase of temperature and the abundance ratio in several cases. We end by making the point that present models for FIP variations involve only the local geometry of the magnetic field (in the region $T \approx 10^4$ K where the segregation occurs according to the FIP of the element), while the present results show that the magnetic topology - a global quantity - may also have an important role.

Acknowledgements

We wish to acknowledge useful discussions with Sarah Gibson and Dick Canfield, and the help of the SOHO-CDS team, in particular Dave Pike. We thank Pawel Rudawy for providing the Bialków observations and Yuan Yong Deng for data processing of Fig. 2. We acknowledge financial support from ECOS (France), PPARC (UK) and ANPCYT (Argentina) through their cooperative science program (A97U01). Part of this work (LF, NN) was carried out under NASA contact NS8-37334 (*Yohkoh*/SXT). SoHO is a project of international collaboration between ESA and NASA. The Yohkoh mission is a project of the Institute of Space and Astronautical Science (ISAS) in Japan. It is financially supported by ISAS, NASA and PPARC. The authors of this paper benefited from discussions at the second SoHO-Yohkoh Coordinated Data Analysis Workshop held in MEDOC, Orsay, France.

References

Aulanier, G., Démoulin, P., van Driel-Gesztelyi, L., Mein, P., DeForest, C. 1998a, Astron. Astrophys. 335, 322.

Aulanier, G., Démoulin, P., Schmieder, B., Fang, C. and Tang, Y.H. 1998b, Solar Phys. 183, 369.
Aulanier, G., Schmieder, B., Kucera, T., van Driel-Gesztelyi, L., Démoulin, P., Mein, N., Vial, J.-C., Mein, P., 1999, in Third Advances in Solar Physics Euroconference: Magnetic Fields and Oscillations, ASP Conference Series vol.184, p. 291-295. Eds. B. Schmieder, A. Hofmann, J. Staude.
Arnaud, M., Rothenflug, R. 1985, Astron. Astrophys. Suppl. series 60, 425.
Bentley, R. D., Klein, K.-L., van Driel-Gesztelyi, L. et al. 2000 *Solar Phys.*, in press.
Berger, T. R., De Pontieu, B., Schijver, C. J., Title, A. M., 1999, Astrophys. J. 519, L97.
Canfield, R. C., Hudson, H. S., & McKenzie, D. E. 1999, Geophys. Res. Lett. 26, 627.
Cheng, C. Z. & Choe G. S. 1998, Astrophys. J. 505, 376.
Delaboudinière, J.P., Artzner, G.E., Brunaud, J., Gabriel, A., Hochedez, J.F. et al. 1995, Solar Phys. 162, 291.
Démoulin, P. & Priest, E.R. 1997, Solar Phys. 175, 123.
Démoulin P., Hénoux J.C., Priest E.R. and Mandrini C.H. 1996, Astron. Astrophys. 308, 643.
Démoulin P., Bagalá L.G., Mandrini C.H., Hénoux J.C. and Rovira, M.G. 1997, Astron. Astrophys. 325, 305.
Deng, Y.Y., Schmieder B., Mandrini, C.H., Khan, J.I., Démoulin, P. and Rudawy, P. 1999, Astron. Astrophys. 349, 927.
Dere, K. P., Landi, E., Mason, H. E., Monsignori-Fossi, B. M. and Young, P. R. 1997, Astron. Astrophys. Suppl. series 125, 149.
Fletcher, L., DePontieu, B. 1999, Astrophys. J. 520, L136.
Gaizauskas, V., Mandrini, C.H., Démoulin, P., Luoni, M.L. and Rovira, M.G. 1998, Astron. Astrophys. 332, 353.
Glover, A., Ranns, N. D. R., Harra, L. K., Culhane, J. L., 2000., Geophys. Res. Lett. 27, $N^0$14, 2161.
Golub, L., Zirin, H. and Wang, H. 1994, Solar Phys. 153, 179.
Hansteen, Maltby & Malagoli 1993, in "Magnetic Reconnection in the Solar Atmosphere", A.S.P. Conference Series no. 111, eds. R. D. Bentley & J. T. Mariska, 116.
Hara, H., Tsuneta, S., Lemen, J.R., Acton, L.W. and Mc Tiernan, J.M. 1992, Publ. Astron. Soc. Japan, 44, L135.
Harrison R. et al. , 1995, Solar Phys. 162, 233.
Howard, R. F., Harvey, J. W. & Forgach, S. 1990, Solar Phys. 130, 295.
Hudson, H. S., et al., 1998, GRL 25, 248
Leka, K.D., Canfield, R.C., McClymont, A.N. and van Driel-Gesztelyi, L. 1996, Astrophys. J. 462, 547.
Lin, R. P. 1987, Rev. Geophys. 25, 676.
Longcope, D. W. 1996, Solar Phys. 169, 91.
López Fuentes, M.C., Mandrini, C.H., Rovira, M.G. and Démoulin, P. 2000, Geofis. Inter. 39, $N^0$1, 65
Low, B.C. 1991, Astrophys. J. 370, 427.
Low, B.C. 1992, Astrophys. J. 399, 300.
Mandrini, C.H., Démoulin, P. and Klimchuk J. 2000, Astrophys. J. 530, 999.
Mandrini, C.H., Démoulin, P., Schmieder, B., Deng, Y.Y. and Rudawy, P. 1999a, ESA-SP 448, 617
Mandrini, C.H., Démoulin, P., van Driel-Gesztelyi, L., Schmieder, B., Cauzzi, G. and Hofmann, A. 1996, Solar Phys. 174, 229.

Mandrini, C.H., Deng, Y.Y., Schmieder, B., Démoulin, P., Rudawy, P., Newmark, J. and DeForest, C. 1999b, Astron. Soc. Pacific C.S. 184, 276

Mandrini C.H., Rovira M.G., Démoulin P., Hénoux J.C., Machado M.E., Wilkinson L.K. 1993, Astron. Astrophys. 272, 609.

Meyer, J.-P. 1985a, Astron. Astrophys. Suppl. series 57, 173..

Meyer, J.-P. 1985b, Astron. Astrophys. Suppl. series 57, 151.

Miller, J. A. & Viñas, A. F. 1993, Astrophys. J. 412, 386.

Nakagawa, Y. 1971, in IAU Symposium 43 , "Solar Magnetic Fields", p 275, Robert Howard (ed.).

Ogawara Y., Takano K., Kato T., Kosugi T., Tsuneta S. et al. 1991, Solar Phys. 136, 1.

Peres, G., Reale, F. & Golub, L., 1994, Astrophys. J. 422, 412.

Pevtsov, A.A., Canfield, R.C., and Metcalf, T.R., 1995, Astrophys. J. 440, L190.

Pevtsov, A. A., Canfield, R. C. & McClymont, A. N. 1997, Astrophys. J. 481, 973.

Rust, D. M., & Kumar, A. 1996, Astrophys. J. 464, L199.

Sakurai, T., Wang, H, in 1998 Proceedings of the Nobeyama Symposium, Kiyosato, Japan, Oct. 27-30, 1998, Eds.: T. S. Bastian, N. Gopalswamy and K. Shibasaki, NRO Report No. 479., p.77-81

Scherrer, P.H., Bogart, R.S., Dush, R.J., et al. 1995, Solar Phys. 162, 129.

Schmieder, B., Aulanier, G., Démoulin, P., van Driel-Gesztelyi L., Roudier T., Nitta N. and Cauzzi G. 1997, Astron. Astrophys. 325, 1213.

Schmieder, B., Démoulin, P., Aulanier, G. and Golub, L. 1996, Astrophys. J. 467, 881.

Seehafer, N. 1986, Solar Phys. 105, 223.

Sheeley, N. R. 1996, Astrophys. J. 469, 423.

Shibata, K. et al. 1992, PASJ 44, L173.

Titov, V.S., Priest, E.R., Démoulin, P. 1993, Astron. Astrophys. 276, 564.

Tsuneta, S., Acton, L.W., Bruner, M., et al. 1991, Solar Phys. 136, 37.

van Ballegooijen, A. A., Nisenson, P., Noyes, R. W.; Lfdahl, M. G., Stein, R. F., Nordlund, . & Kishnakumar, V. 1998, Astrophys. J. 509, 435.

van Driel-Gesztelyi, L. 1998, in C. E. Alissandrakis & B. Schmieder (eds.), ASP Conf. Ser. 155, 202

Wang, T., Wang, H., Qiu, J. 1999, Astron. Astrophys. 342, 854.

Yokoyama, T. & Shibata, K. 1995, Nature 375, 44.

Young, P. R. & Mason, H. E. 1997, Solar Phys. 175, 523. Young, P. R. & Mason, H. E. 1998, Sp.Sci.Revs 85, 315.

Table I. Intensities in ergs $cm^{-2}s^{-1}sterad^{-1}$, averaged over a number of pixels the low temperature lines of Ne and Mg on June 3. For a given feature, the first line is at 14:09:19 UT and the second line at 15:39:10 UT.

Feature	Ne IV 543.9 Å	Ne V 572.3 Å	Ne VI 562.8 Å	Mg V 353.2 Å	Mg VI 349.2 Å
A	7.6±0.7	15.8±0.5	26.3±0.3	21.8±2.8	37.5±5.2
	2.3±0.2	6.0±0.2	10.8±0.1	7.3±0.9	10.5±1.5
B	6.0±0.6	16.2±0.5	37.9±0.4	12.7±1.6	28.9±4.0
	7.3±0.7	22.0±0.7	45.8±0.5	18.1±2.4	36.5±5.1
C	4.6±0.5	10.9±0.3	26.8±0.3	17.1±0.6	30.6±4.3
	6.0±0.6	18.7±0.6	51.3±0.5	33.5±4.4	78.2±11.0
D	16.6±1.6	21.2±0.6	32.8±0.3	<4.3	17.1±2.4
	9.6±1.0	12.1±0.4	20.5±0.5	109.9±14.2	12.2±1.7
E	5.0±0.5	9.5±0.3	30.2±0.3	12.5±1.6	31.2±4.4
	11±1.1	12.8±0.4	40.9±0.4	65.4±8.5	51.8±7.3

Table II. Intensities in ergs $cm^{-2}s^{-1}sterad^{-1}$, averaged over a number of pixels in the low temperature lines of Ne and Mg on June 4 and 5 for the only feature present (B).

Date	Ne IV	Ne V	Ne VI	Mg VI	Mg VI
4, 12:16:58	21 ± 1	67 ± 2	163 ± 3	73 ± 2	153 ± 2
4, 14:11:26	14 ± 1	43 ± 1	111 ± 2	42 ± 1	66 ± 2
5, 12:36:33	12 ± 1	43 ± 1	102 ± 2	35 ± 1	68 ± 8
5, 15:02:13	15 ± 1	63 ± 2	180 ± 4	91 ± 3	199 ± 4

Table III. Mg VI/Ne VI ratio, Mg VII density diagnostic ratio, electron number density, in units of $10^9\mathrm{cm}^{-3}$ and Mg/Ne abundance ratio on June 3, 4 and 5. For a given feature on June 3, the first line is at 14:09:19 UT and the second line at 15:39:10 UT, for June 4 at 12:16:58 UT and 14:11:26 UT, for June 5 at 12:36:33 UT and 15:02:13 UT, respectively. Note, the error on the density is a blanket 25% error to take into account the unknowns in atomic data. Typically this is larger than that generated by observational errors.

Date	Feature	$\frac{I_{349.2}}{I_{562.8}}$	$\frac{I_{319.0}}{I_{367.7}}$	$n_e(10^9\mathrm{cm}^{-3})$	$\frac{Ab_{Mg}}{Ab_{Ne}}$
June 3	A	1.44 ± 0.10	0.65 ± 0.10	$3.2^{+0.8}_{-0.6}$	3.2 ± 0.7
	A	0.97 ± 0.07	0.80 ± 0.18	5.7 ± 1.0	2.0 ± 0.4
	C	1.07 ± 0.12	0.71 ± 0.09	$4.1^{+0.8}_{-0.7}$	2.3 ± 0.5
	C	1.53 ± 0.17	0.74 ± 0.08	$4.7^{+0.8}_{-0.7}$	3.2 ± 0.7
	E	1.11 ± 0.08	0.64 ± 0.07	3.1 ± 0.5	2.5 ± 0.5
	E	1.78 ± 0.13	0.57 ± 0.09	2.4 ± 0.4	3.9 ± 0.8
	D	0.56 ± 0.08	0.78 ± 0.09	5.3 ± 0.4	1.2 ± 0.4
	D	0.59 ± 0.08	0.57 ± 0.08	2.4 ± 0.4	1.3 ± 0.4
	B	0.77 ± 0.06	0.55 ± 0.08	2.2 ± 0.5	1.7 ± 0.4
	B	0.80 ± 0.06	0.62 ± 0.11	2.9 ± 0.6	1.7 ± 0.4
June 4	B	0.9 ± 0.02	0.7 ± 0.02	3.2 ± 0.8	1.1 ± 0.3
	B	0.6 ± 0.02	0.6 ± 0.02	2.4 ± 0.6	0.7 ± 0.2
June 5	B	0.6 ± 0.02	0.6 ± 0.04	2.4 ± 0.6	0.8 ± 0.2
	B	1.0 ± 0.03	0.6 ± 0.02	3.0 ± 0.8	1.2 ± 0.3

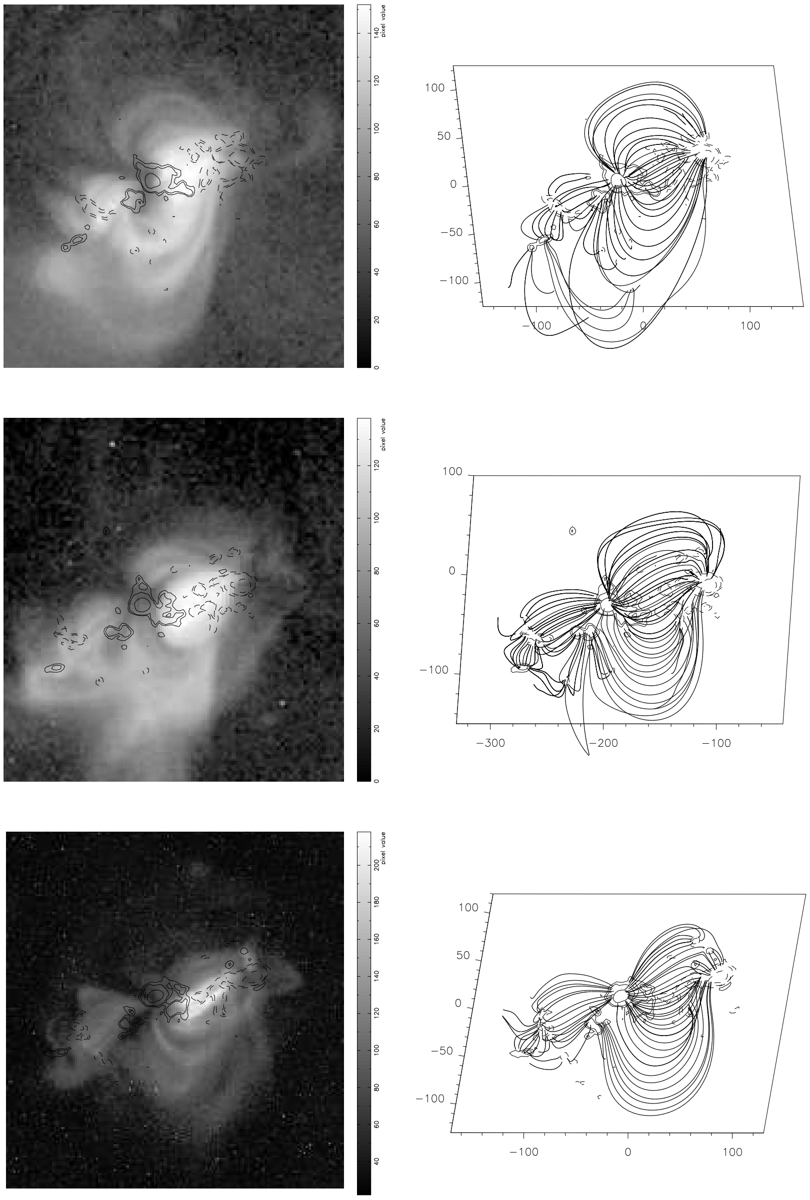

Figure 1. SXT images in Al12 filter (left column). The top row corresponds to June 3 at 14:08 UT, the central row to June 4 at 14:25 UT and the bottom row to June 5 at 14:08 UT. The images have been overlaid to MDI magnetograms for comparison with the magnetic model (right panels). The MDI magnetograms used correspond to June 3, 14:28 UT (top row), June 4, 12:52 UT (central row) and June 5, 11:16 UT (bottom row). The isocontours of B_l are $\pm$ 50, 100 and 500 G, positive (negative) values are drawn in continuous (dashed) line. A set of field lines has been added in every map to be compared with the SXT data. The sizes of the frames are expressed in Mm and the trapezoidal shape is due to the effect of projection.

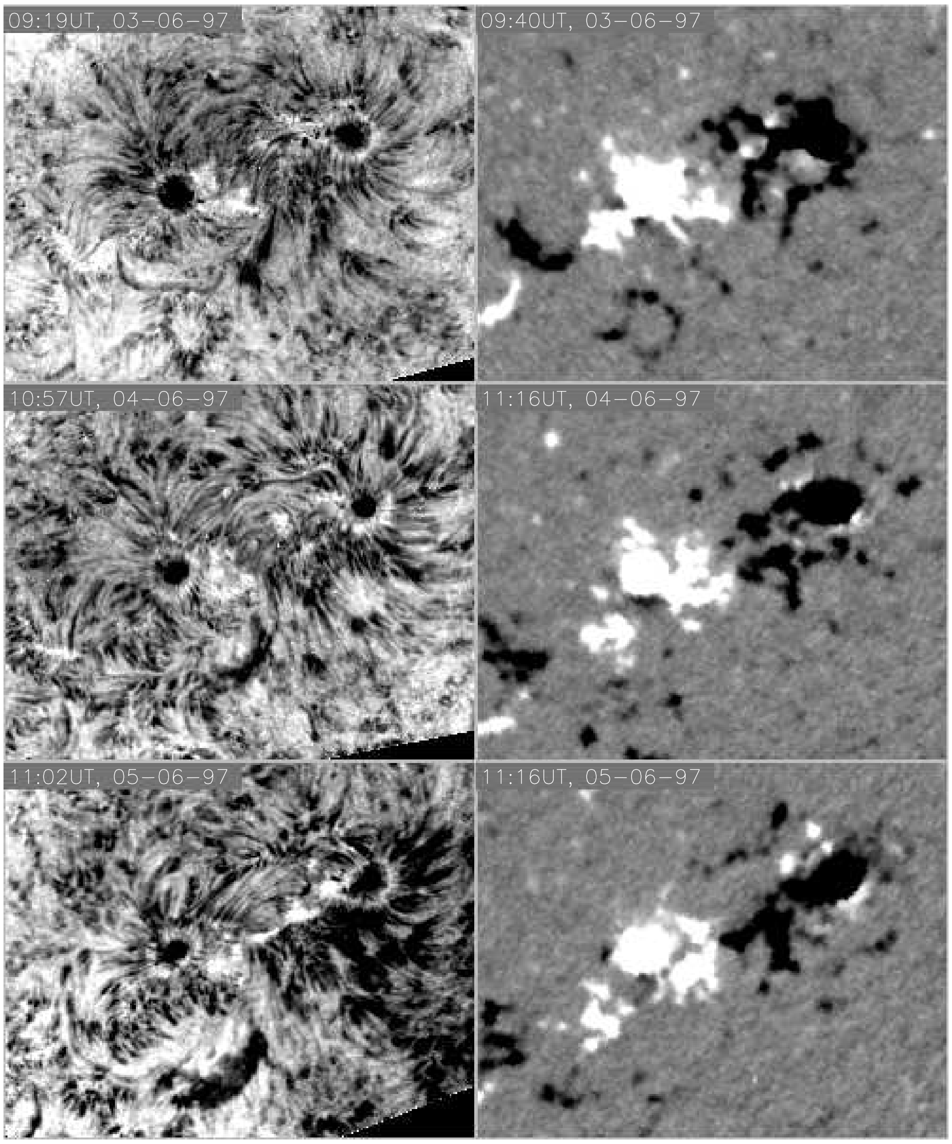

Figure 2. Hα images of Bialków (left panels) and MDI magnetograms (right panels) for June 3, 4, 5, 1997. The size of the image is $\approx$ 282" in x and 225" in y. Black (white) represent negative (positive) polarities of the longitudinal field, respectively.

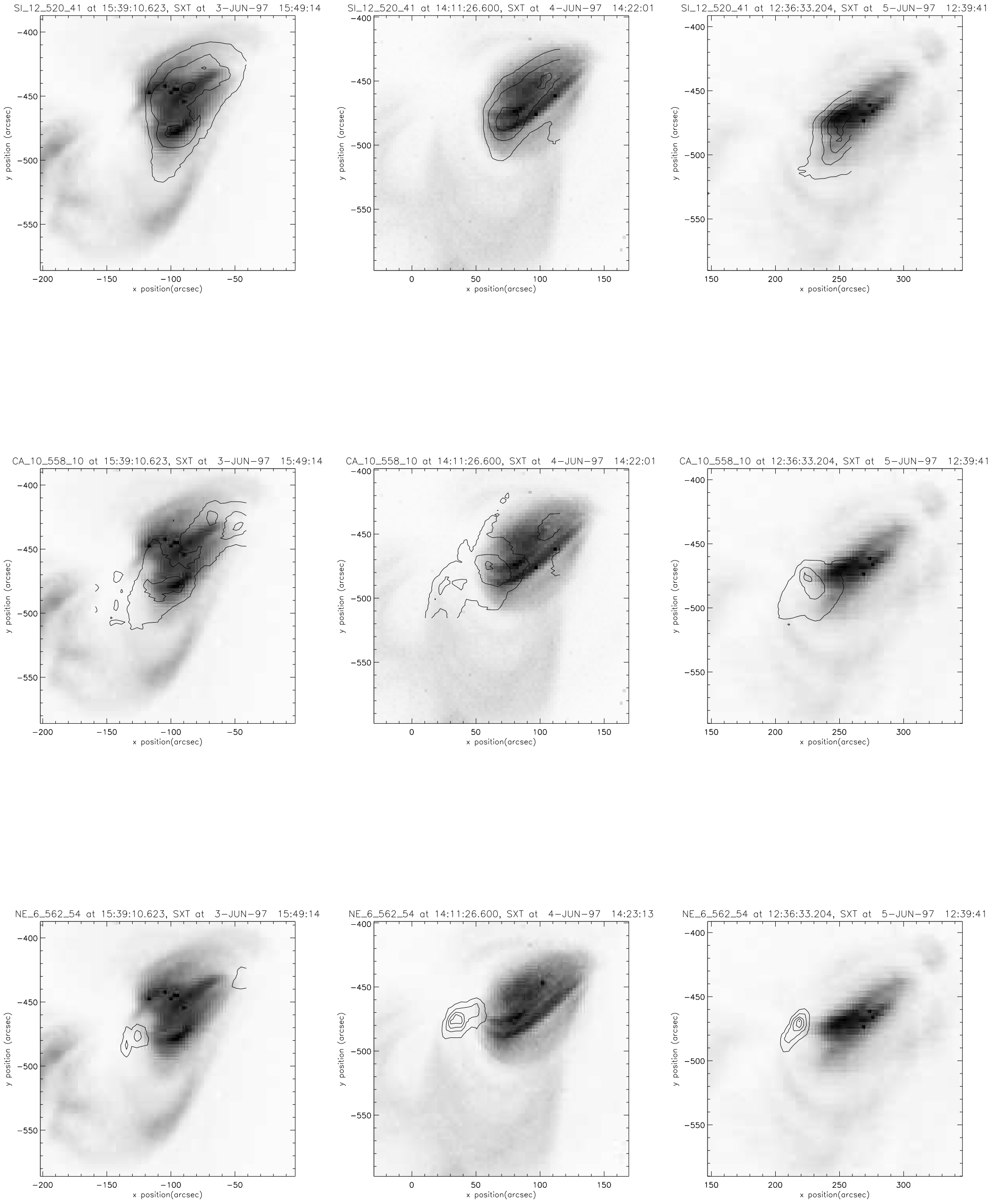

Figure 3. Overlays of SXT AlMg filter image with CDS rasters: Si XII emission (T $= 2.10^6$K first row), Ca X 557.8 Å emission (T $= 10^6$K, middle row) and Ne VI 562.8 Å emission (T = 400,000K, low row). The Si XII emission follows the bright core of the SXT emission. Ca X emission maps part of the core loops and footpoints, and Ne VI emission is concentrated at the footpoints of the large, diffuse SXT loops. Note that in the observations of June 4, 5 the CDS raster does not extend to the North end of the SXT loop system.

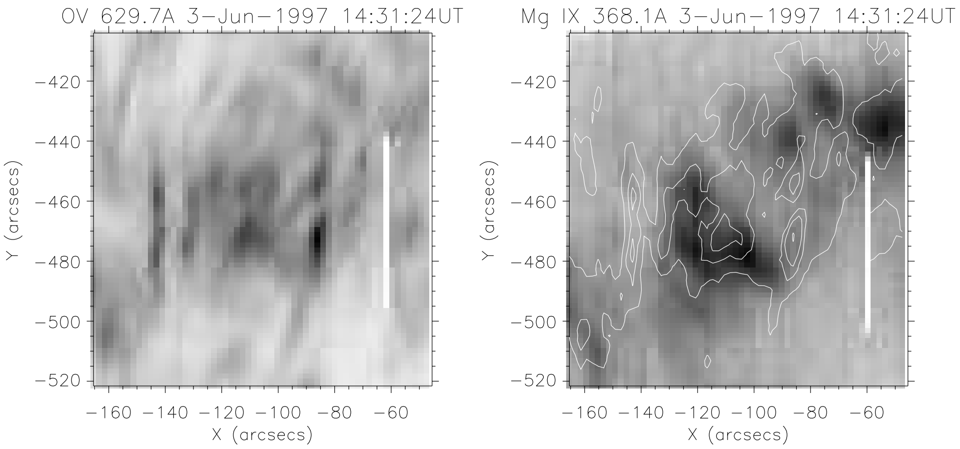

Figure 4. AR8048 viewed in O V 629.7 Å a transition region line formed at 0.25 MK, and Mg IX at 368.1 Å a transition region/coronal line formed at 1MK, illustrating the difference in the type of structure observed. At 0.25MK, emission is concentrated into small bright blobs and elongated structures, while at 1MK, emission is far more widespread and diffuse

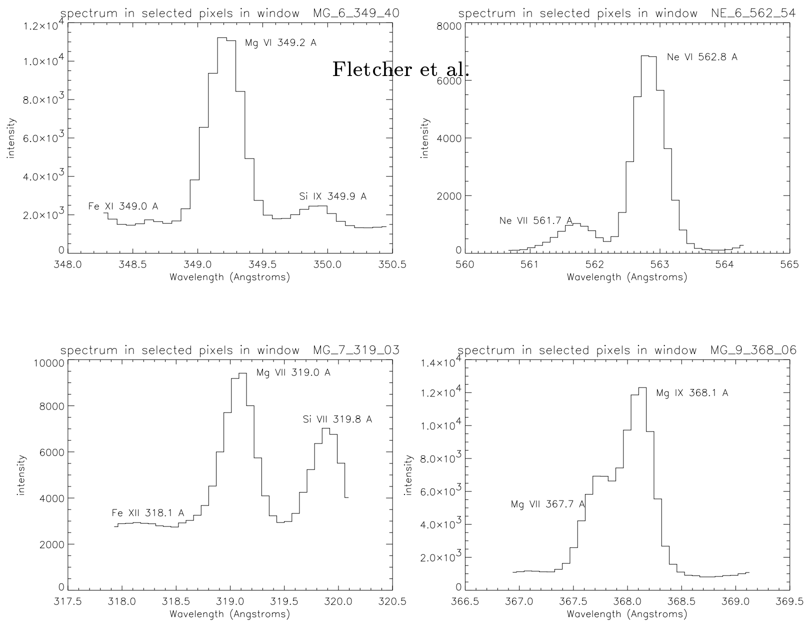

Figure 5. Spectra in the summed pixels in the bright Ne/Mg feature at (35, -475) on June 4, 1997, 12:16:58 UT (see Fig. 3) with line identifications. Shown are the Mg VI and Ne VI windows from which the intensity ratio is measured, and the Mg VII and Mg IX windows containing the Mg VII density diagnostic pair.

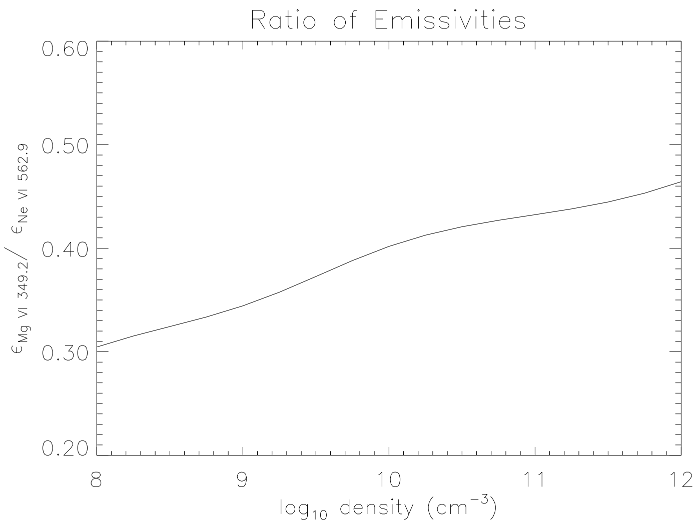

Figure 6. The variation with electron number density of the theoretical emissivity ratio ($\Delta E n_i A_j i$) in the Mg VI 349.16 + 349.18 Å lines and the Ne VI 562.7 + 562.8 Å lines, calculated using atomic data from the CHIANTI (v2.0) database

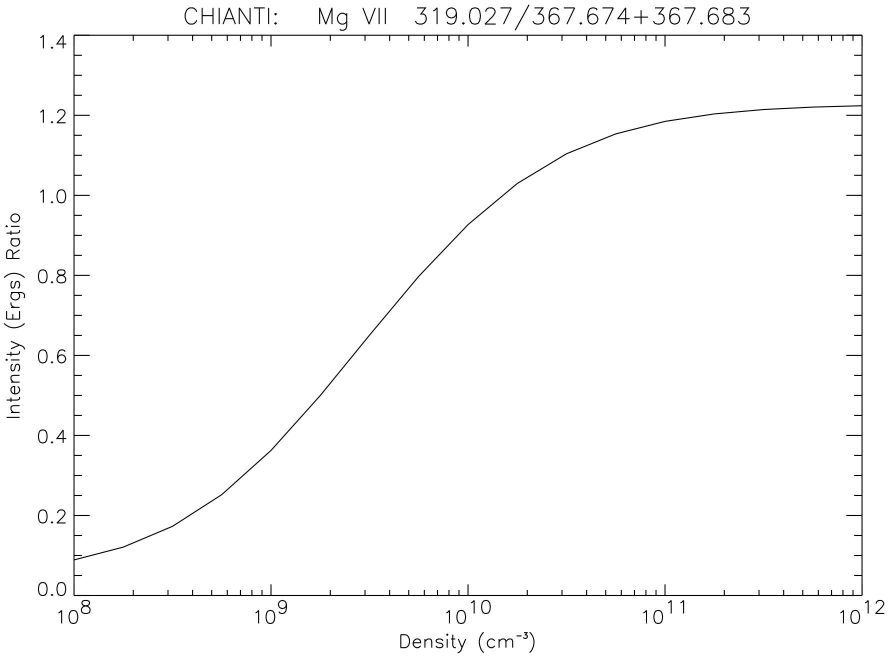

Figure 7. The Mg VII intensity ratio as a function of electron number density, at a temperature of 0.63 MK as predicted with atomic data from the CHIANTI (v2.0) data base.

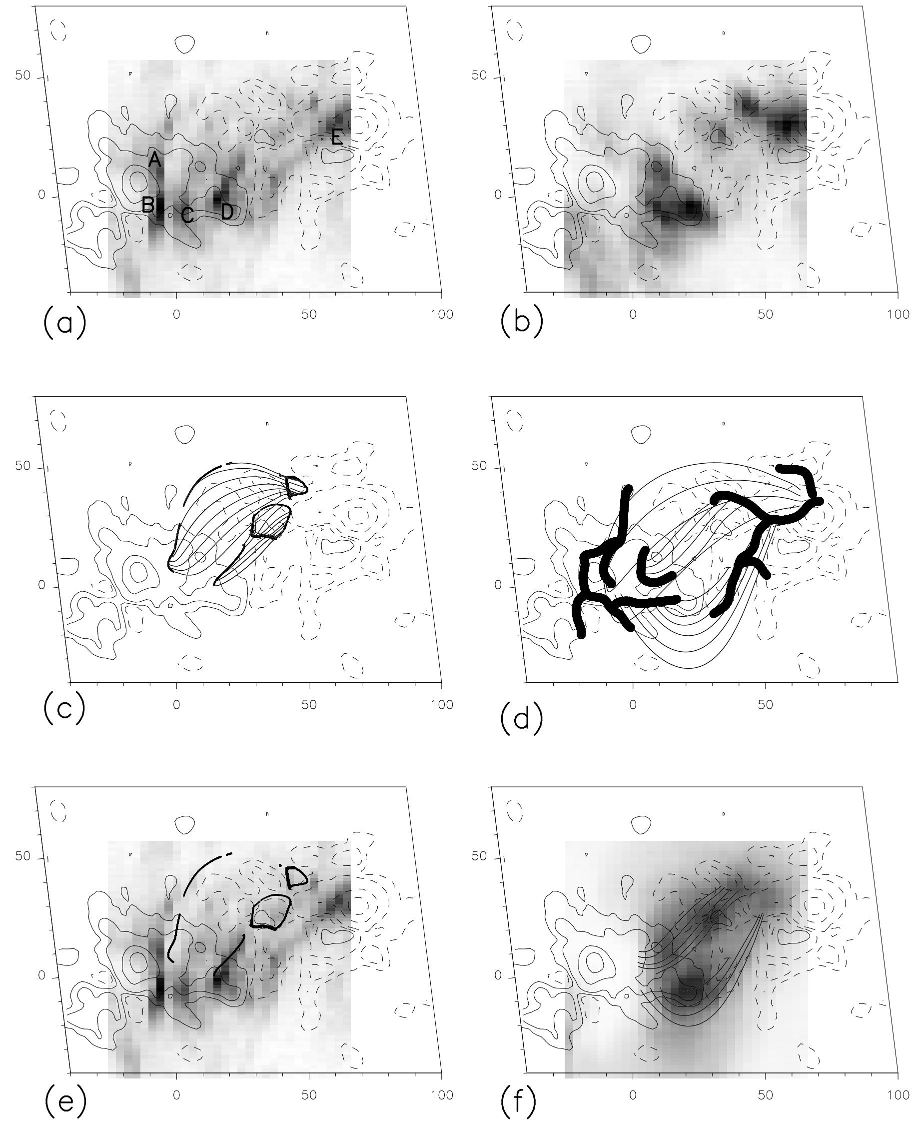

Figure 8. A comparison of the magnetic topology and CDS data for June 3. (a) and (b) are, respectively, an overlay of Ne VI and Mg IX (reversed images) observations at 14:09:39 UT with the MDI magnetogram in Fig. 1. In this case the isocontours of B_l are ± 20, 100, 250, 500, 1000 G, positive (negative) values are drawn in continuous (dashed) lines. We have labeled the Ne VI features in (a). (c) shows the locations of BPs, and the intersection of their separatrices with the photosphere. BPs (separatrices) are drawn in continuous thick (thin) black lines, associated field lines have been added. (d) shows the intersection of QSLs (thick lines) with the photosphere, some field lines issued from QSLs are drawn. In (e) we show only the BPs and their separatrices to point out their closeness to Ne VI brightenings, while in (f) it can be seen how the lines issued from the QSLs lying close to the Mg IX emission outline the shape of the Si XII emission (ovelaid reversed image) at the core of the AR. The convention for the size and shape of the frames is the same as in Fig. 1.

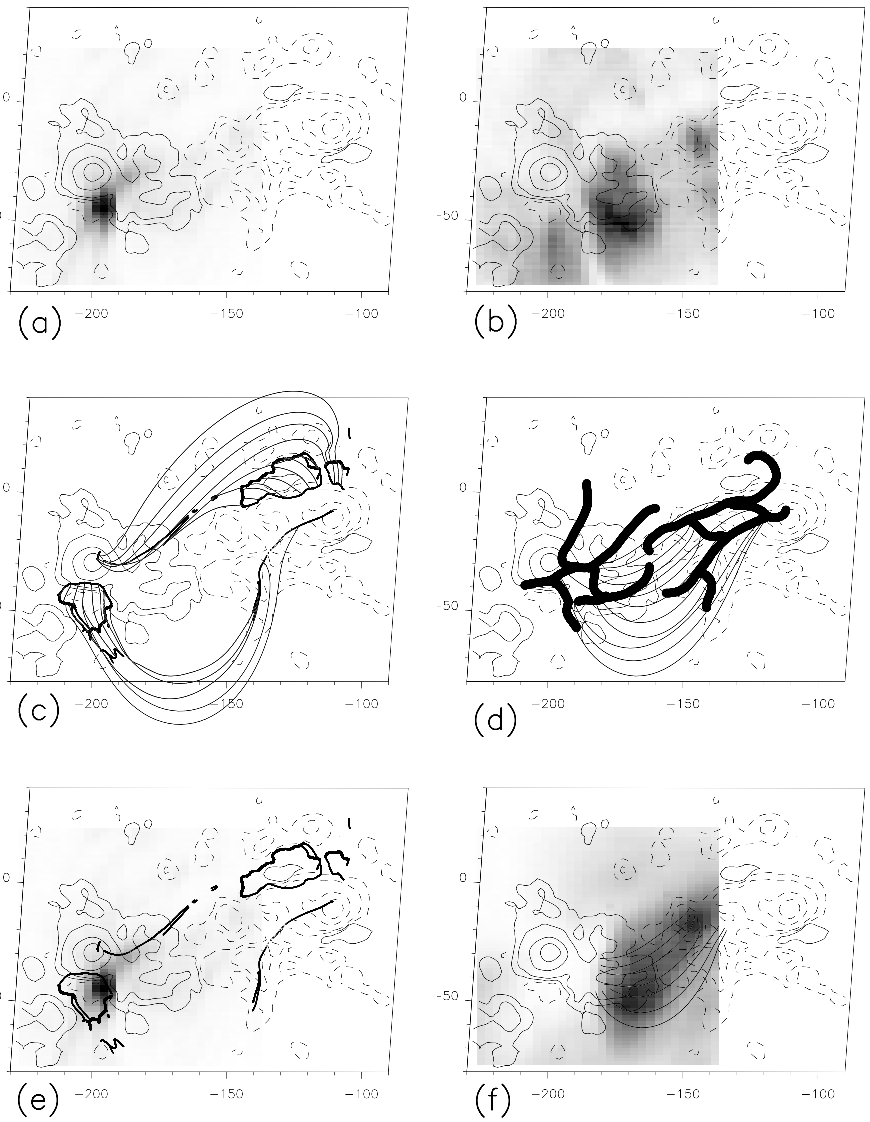

Figure 9. Idem Figure 8 for June 4.

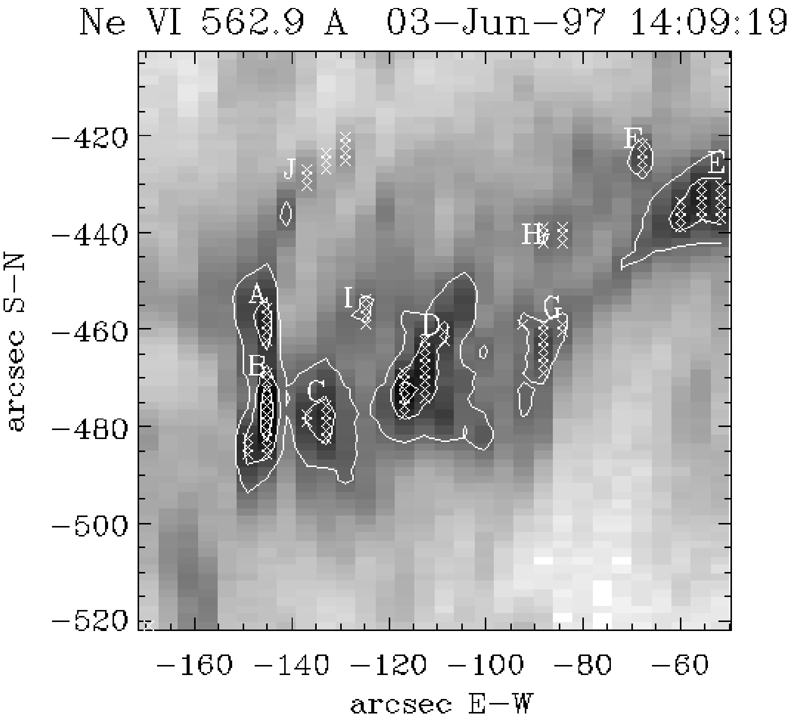

Figure 10. The full set of sources for which abundance measurements were made.

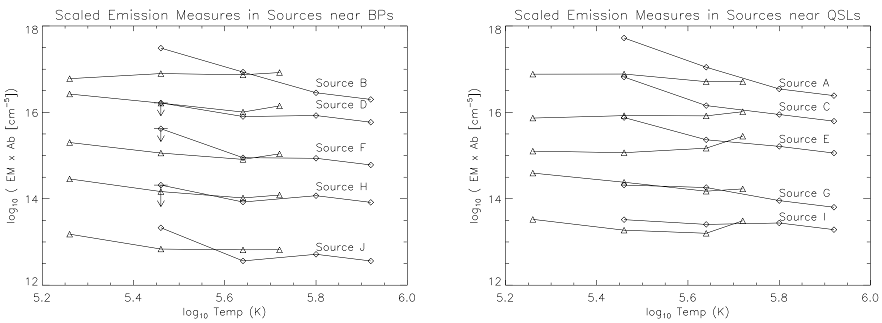

Figure 11. The (scaled) product of emission measure $\times$ abundance as a function of temperature, in various lines of Mg and Ne. The difference between the pair of lines for each source indicates the effect of abundance enhancements. Values for Mg are shown with diamonds, Ne is shown with triangles. Note that the values derived from Mg V (at $\log_{10}(T_e)$= 5.5) are *upper limits* in the case of Features D, F, G, and H, as the Mg V 353.3Å line was too faint to fit reliably in these cases